Indian Journal of Pure & Applied Physics
Vol. 64, March 2026, pp. 304-315
DOI: 10.56042/ijpap.v64i3.26387

Solar and Interplanetary Sources of Major Geomagnetic Storms: Case Studies from Solar Cycle 24 (2008–2019)

Palak Singh Thakur[a], Saket Kumar[a], Swapnil Garg[a], Gauri Richharia[b] & Omkar Prasad Tripathi[a*]

[a]Department of Physics, AKS University, Satna 485 001, India

[b]Department of Electrical Engineering, AKS University, Satna 485 001, India

Received: 9th December 2025; accepted: 3rd February 2026

Geomagnetic storms represent significant space weather phenomena with the potential to disrupt critical technological infrastructure, including communication satellites, navigation systems, and terrestrial power grids. This study presents a descriptive analysis of the four most geo-effective geomagnetic storms of Solar Cycle 24 (2008–2019), a cycle noted for its unusually low activity. The heliospheric drivers of these events are investigated by correlating solar and interplanetary data with the disturbance storm time (Dst) index. The analysed storms, including the notable "St. Patrick's Day" storm of 17 March 2015, as well as events on 23 June 2015, 20 December 2015, and 26 August 2018, were selected based on their intensity (Dst ≤ -150 nT). Our analysis reveals that the primary drivers were interplanetary coronal mass ejections (ICMEs) and their preceding sheath regions. A key insight from this study is the diversity of the storm drivers; major storms were initiated not only by fast CMEs but also by slower CMEs with highly geo-effective magnetic field configurations. Specifically, the prolonged duration of a strong southward interplanetary magnetic field component (Bz) was identified as the crucial factor determining the magnitude of each storm, underscoring that forecasting models must prioritise the analysis of in-transit CME magnetic structure over initial kinematics to improve the prediction of severe storm impacts.

Keywords: Geomagnetic storms, Coronal mass ejections, Solar cycle 24, Interplanetary magnetic field, Space weather

1 Introduction

The Earth's magnetosphere is a dynamic system profoundly influenced by the Sun's activity. Transient solar phenomena, such as solar flares (SFs) and coronal mass ejections (CMEs), release vast amounts of plasma and magnetic energy into the heliosphere[1,2]. When these disturbances propagate through interplanetary space as interplanetary CMEs (ICMEs, as illustrated in Fig. 1), they can cause major reconfigurations of the magnetosphere upon arrival at Earth, resulting in geomagnetic storms[3]. These storms are characterized by a significant depression in the horizontal component of the Earth's magnetic field, quantified by the disturbance storm time (Dst) index[4].

The geo-effectiveness of an ICME is primarily determined by the state of its embedded magnetic field[5]. A strong and sustained southward component of the interplanetary magnetic field (IMF Bz) facilitates magnetic reconnection at the dayside magnetopause, efficiently transferring energy from the solar wind into the magnetosphere[6]. This energy transfer drives the storm-time ring current, leading to the observed depression in the Dst index[7]. Such conditions are often found within the compressed plasma of the sheath region preceding an ICME or within the magnetic cloud (MC) structure of the ICME itself[8,9].

Solar Cycle 24 (SC24; December 2008 – December 2019) was the weakest cycle in over a century in terms of sunspot number and magnetic flux, leading to a diminished heliospheric pressure and a generally less disturbed interplanetary medium[10,11]. This unique environment raises critical questions about the nature of severe space weather during periods of low solar activity. While the frequency of large CMEs was reduced[12], the cycle still produced several intense geomagnetic storms, including the notable "St. Patrick's Day" storm on 17 March 2015 (Dst = -223 nT)[13,14]. This apparent contradiction of major storms from a weak Sun suggests that during SC24, the geo-effectiveness of CMEs became less dependent on their raw kinematic power and more critically dependent on the specific configuration of their internal magnetic fields[15], as well as their interactions with the altered ambient solar wind[16,17]. Studies indicate that slower CMEs could be more effectively preconditioned and compressed by the structured, low-density solar wind of SC24, enhancing their magnetic drivers at 1

*Corresponding author: E-mail: omkar8415@gmail.com

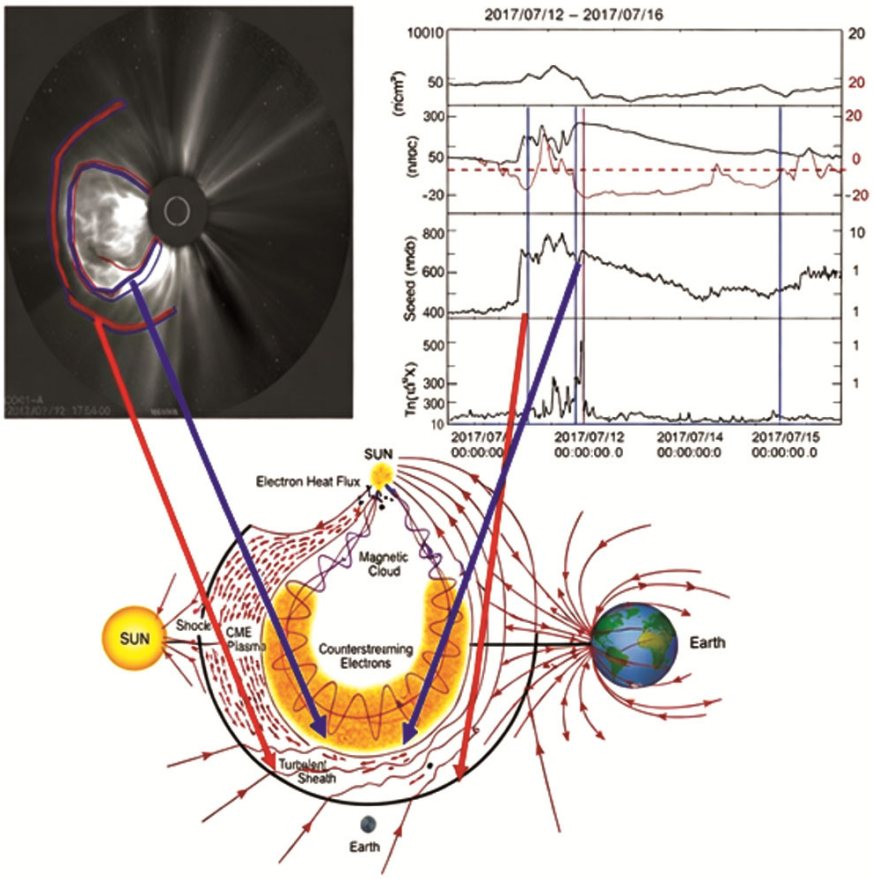

Fig. 1 — CME-driven geomagnetic storm dynamics. Panels show coronagraph observations (left), in-situ solar wind/IMF signatures (right), and a conceptual model of the turbulent sheath and magnetic cloud (bottom)

AU[18,19]. Therefore, SC24 provides a crucial test case for understanding how CME magnetic structure, rather than speed alone, governs extreme space weather[20].

This paper presents a descriptive study of the four most significant geomagnetic storms of SC24 with Dst ≤ -150 nT. By analysing the associated solar phenomena and *in-situ* interplanetary plasma and field data, we aim to identify the specific heliospheric structures responsible for each storm's intensity. Our analysis seeks to elucidate the distinct mechanisms that led to major geomagnetic disturbances within a weak solar cycle, providing new insights into the parameters that control geo-effectiveness in different heliospheric environments.

2 Materials and Methods

To investigate severe geomagnetic storms during Solar Cycle 24 (SC24), a comprehensive multi-source dataset was employed, integrating geomagnetic indices, *in-situ* solar wind plasma measurements, interplanetary magnetic field (IMF) observations, and coronal mass ejection (CME) information. The hourly disturbance storm time (Dst) index, a standard and widely accepted quantitative measure of geomagnetic storm intensity, was obtained from the SPDF OMNIWeb database maintained by the World Data Center for Geomagnetism, Kyoto[21]. High-resolution (1-minute) solar wind plasma and IMF data were acquired from the NASA/GSFC OMNIWeb database, basedon observations from the *Wind* and *ACE* spacecraft and time-shifted to the Earth's bow shock nose, ensuring accurate representation of upstream solar wind conditions relevant to solar wind–magnetosphere coupling[22].

The present study focuses exclusively on geomagnetic storms with minimum Dst ≤ −150 nT. This threshold was deliberately chosen to isolate severe and highly geo-effective storms, following well-established storm classification schemes in which storms with Dst ≤ −100 nT are categorised as intense, while events exceeding ≤−150 nT represent extreme disturbances driven by sustained and strong solar wind forcing[23-25]. Previous studies have shown that storms below this threshold are more frequently

associated with prolonged southward IMF Bz, enhanced solar wind electric fields, and efficient ring current intensification, making them particularly suitable for investigating solar wind driver–storm relationships[26-28]. Storms with minimum Dst values close to but weaker than −150 nT were intentionally excluded to maintain homogeneity in storm intensity and to avoid ambiguity arising from mixed or weaker interplanetary drivers, which are more common in moderately intense storms[29]. This strict selection criterion ensures that the analyzed events represent a coherent population of extreme storms dominated by robust solar wind–IMF structures. Based on this criterion, four major geomagnetic storms during SC24 were selected for detailed analysis: (i) 17 March 2015, (ii) 23 June 2015, (iii) 20 December 2015, and (iv) 26 August 2018.

Information on CME properties, including launch time, linear speed, angular width, and classification as halo or partial-halo CMEs, was obtained from the SOHO/LASCO CME catalog, which provides a comprehensive and systematically compiled record of CMEs observed by the LASCO coronagraph[30,31]. The identification of interplanetary shocks and their association with magnetic cloud (MC) structures was further supported using the Heliospheric Shock Database maintained by the University of Helsinki, which offers reliable shock timing and classification essential for interplanetary structure analysis[32,33].

For each selected storm, detailed time series analyses were performed for key interplanetary parameters, including the total IMF strength (B), the north–south component of the IMF (Bz), solar wind proton density (Dsw), solar wind speed (Vsw), plasma temperature (Tsw), and solar wind dynamic pressure (Psw). To establish quantitative relationships between solar wind conditions and geomagnetic activity, correlation analyses were carried out between the Dst index and primary solar wind drivers such as Bz, Vsw, and the interplanetary electric field (Ey). In addition, event-wise peak values, main-phase averages, and the duration of sustained southward IMF Bz were evaluated and compared across events to quantify the relative geoeffectiveness of different interplanetary structures[34-36].

The relative contributions of sheath and magnetic cloud (MC) regions to storm development were identified using a systematic, objective, and reproducible methodology based on well-established physical criteria from both classical and recent literature. Sheath regions, located between the interplanetary shock and the leading edge of the ejecta, were identified by enhanced solar wind proton density and temperature, elevated dynamic pressure, increased plasma beta, and highly fluctuating magnetic fields, indicative of strong compression and turbulence. In contrast, magnetic cloud intervals were identified by smooth and coherent magnetic field rotation, enhanced magnetic field magnitude, low plasma beta, and reduced proton temperature relative to expected solar wind values, consistent with classical MC definitions[37-38]. The initial, main, and recovery phases of each geomagnetic storm were delineated using the temporal evolution of the Dst index following standard storm-phase definitions[39]. These storm phases were then systematically mapped onto the identified sheath and MC intervals to determine the dominant interplanetary drivers responsible for the main phase intensification. This approach enables a clear separation between storms primarily driven by compressed and fluctuating sheath fields and those dominated by prolonged southward magnetic fields within magnetic clouds, which are known to be the principal drivers of intense and long-duration geomagnetic storms[40,41].

3 Results and Discussion

Our analysis examines the solar origins and interplanetary drivers of the four selected major geomagnetic storms from SC24.

3.1 The "St. Patrick's Day" Storm: 17 March 2015

The St. Patrick's Day geomagnetic storm of 17–18 March 2015 was the most severe space-weather event of Solar Cycle 24, reaching a minimum Dst of −223 nT and attaining G4 (severe) storm conditions (Kp = 8; Fig. 2 (b)). In the context of historical geomagnetic activity, Solar Cycle 24 was anomalously weak, with relatively few occurrences of Kp ≥ 8, emphasizing the exceptional nature of this event (Fig. 2 (d)). The storm was initiated by a partial-halo coronal mass ejection (CME) launched on 15 March 2015 at 02:48 UT from NOAA Active Region 12297 (Fig. 2 (a)). The eruption, associated with an M-class solar flare, was observed by SOHO/LASCO and had an initial speed of approximately 745 km s^{-1}, accompanied by Type II radio emission indicative of shock formation (Fig. 2 (c)). The resulting interplanetary (IP) shock arrived at the Wind spacecraft at ~04:00 UT on 17 March, producing a well-defined sudden storm commencement (SSC).

The geomagnetic storm evolved through a classical two-step main phase. The first phase was driven by the

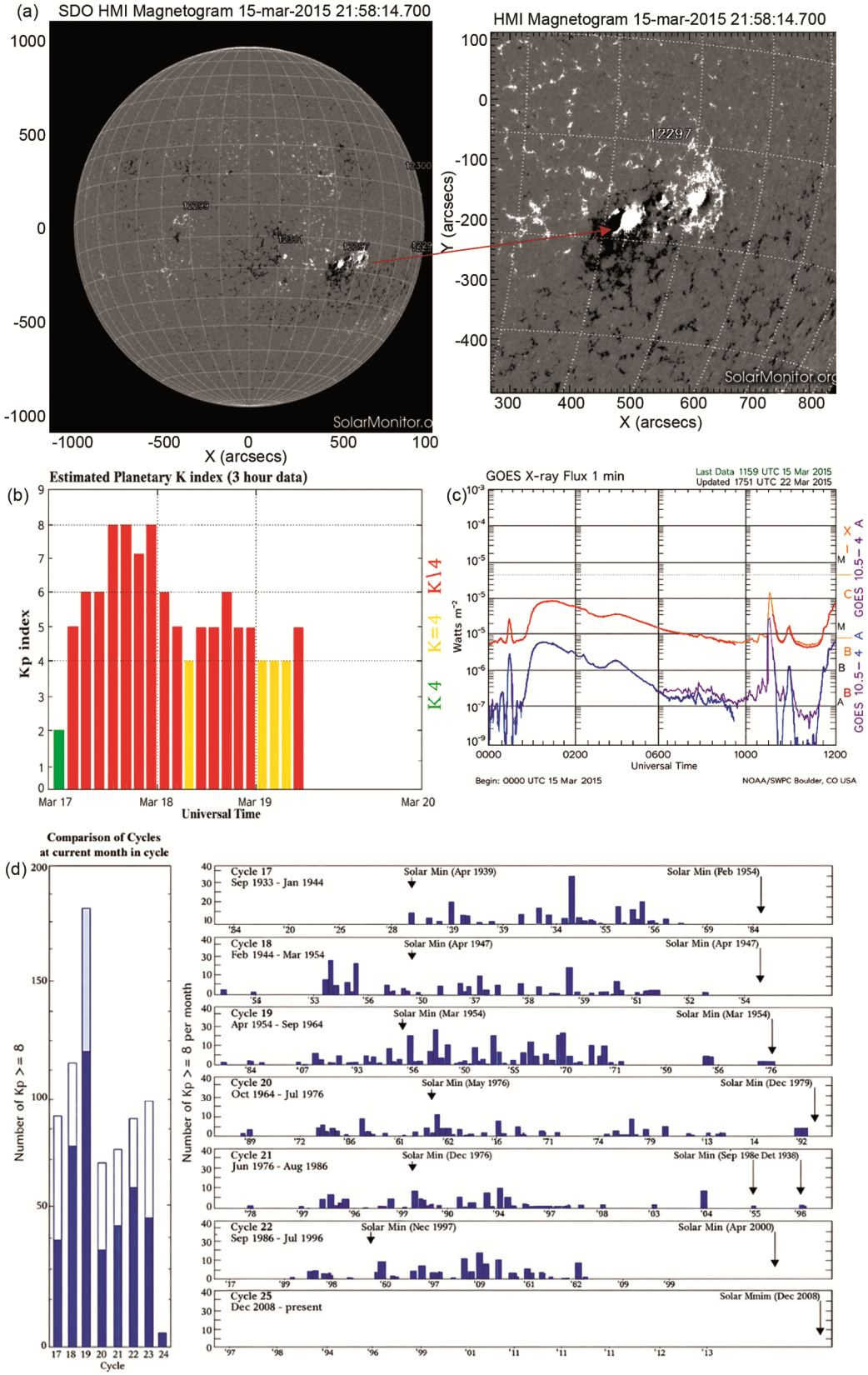

Fig. 2 — Overview of the 17–18 March 2015 geomagnetic storms. (a) NOAA AR 12297, (b) Kp index, (c) GOES X-ray flux, and (d) historical occurrence of Kp≥8 events

compressed sheath region immediately behind the IP shock, during which the interplanetary magnetic field (IMF) intensity exceeded 30 nT and Bz fluctuated strongly southward, reaching values near −26 nT. This interval coincided with sharp enhancements in solar-wind density, velocity, and dynamic pressure, leading to an initial intensification of geomagnetic activity. The second and more intense phase began with the arrival of a magnetic cloud (MC), characterized by a prolonged and coherent interval of strong southward IMF, which enabled efficient solar-wind–magnetosphere coupling and ultimately produced the geomagnetic superstorm.

A single magnetic cloud (MC17) is identified as the driver of the IP shock (Shock17) observed on 17 March 2015. The MC identification was performed using a two-step methodology. First, an automatic magnetic-cloud identification (MCI) algorithm was applied to detect MC candidates[42]. Subsequently, a magnetic-cloud fitting (MCF) model based on a force-free flux-rope formulation was used to derive the MC's physical parameters[43]. Figure 3 presents the temporal evolution of the interplanetary magnetic field, solar-wind plasma parameters, the Dst index, and selected derived quantities during 17–18 March 2015. The MC candidate detected by the MCI model is marked by a horizontal black bar, while the MC interval determined by the MCF model (MC17) is bounded by two vertical red lines (Fig. 3 (d)). The visually identified rear boundary of MC17 agrees well with the MCI result, whereas the front boundary determined visually precedes the MCI boundary by approximately 4 h. The shock driven by MC17 (Shock17) is indicated by a vertical line in Fig. 3[44].

Wind observations further reveal an extended interval of low plasma-beta (β) solar-wind material lasting approximately 24 h, from ~12:00 UT on 17 March to ~12:00 UT on 18 March. This low-β interval is interrupted by a magnetic hole near the end of 17 March, as indicated in Fig. 3[45]. Following the rear boundary of MC17, an additional ~12 h low-β interval is observed (marked in orange and labeled "ICME?" in Fig. 3 (b)). However, the MCF model does not yield a reliable fit for this region because the magnetic-field direction shows little systematic rotation (i.e., minimal variation in θB and φB), and Bz remains close to zero throughout the interval. The lack of coherent field rotation and sustained southward IMF suggests that this region does not represent a distinct magnetic cloud, but likely constitutes a post-MC solar wind stream with a compressed magnetic field[38].

Based on these results, the 17 March 2015 geomagnetic superstorm is concluded to have been driven by southward IMF contributions from both the sheath region and a single magnetic cloud, MC17[13]. Our findings are consistent with previous results but differ from the interpretations in research papers[46]. Specifically, one study identified an MC interval nearly twice as long as MC17, while another[47] proposed the presence of two ICMEs, both interpreted as flux ropes using a Grad–Shafranov reconstruction technique[48]. The presence of a magnetic hole within the fitting interval can complicate force-free MC fitting and may account for the discrepancies between those results and our own. Variations in fitting methodology and interval selection are therefore likely responsible for the differing interpretations[49].

The geo-space impacts of the storm were global in extent. High-latitude regions including Scandinavia, northern Russia, Iceland, northern Canada, and Alaska experienced the most intense geomagnetic activity, with strong substorms and clear signatures of geomagnetically induced currents (GICs)[50]. At mid-latitudes, bright auroral displays were observed across much of Europe and North America, extending as far south as Colorado, a consequence of significant ring-current injection and subsequent storm-time ionospheric heating[51,52]. Even at low and equatorial latitudes, the storm produced significant ionospheric disturbances, including pronounced total electron content (TEC) variability and GNSS scintillation, highlighting the global ionospheric response to high-latitude energy input[53,54].

Despite its intensity, the storm did not result in widespread power-grid failures, in contrast to the March 1989 Quebec event[55]. Operational reports indicated localized GIC levels of up to ~200 mV km^{-1} in some high-latitude power networks, sufficient to challenge voltage regulation or trigger protective responses, particularly in regions such as the Kola Peninsula, but without cascading outages[56]. Additional impacts included degradation of HF radio communication, reduced GNSS positioning accuracy, and intermittent loss-of-lock events due to enhanced ionospheric irregularities[57]. Owing to its well-defined interplanetary drivers and strong magnetospheric and ionospheric responses, the 17 March 2015 storm has become one of the most extensively studied events of Solar Cycle 24, providing valuable insights into storm–time coupling processes, GIC generation, ionospheric dynamics, and space-weather forecasting[58,59].

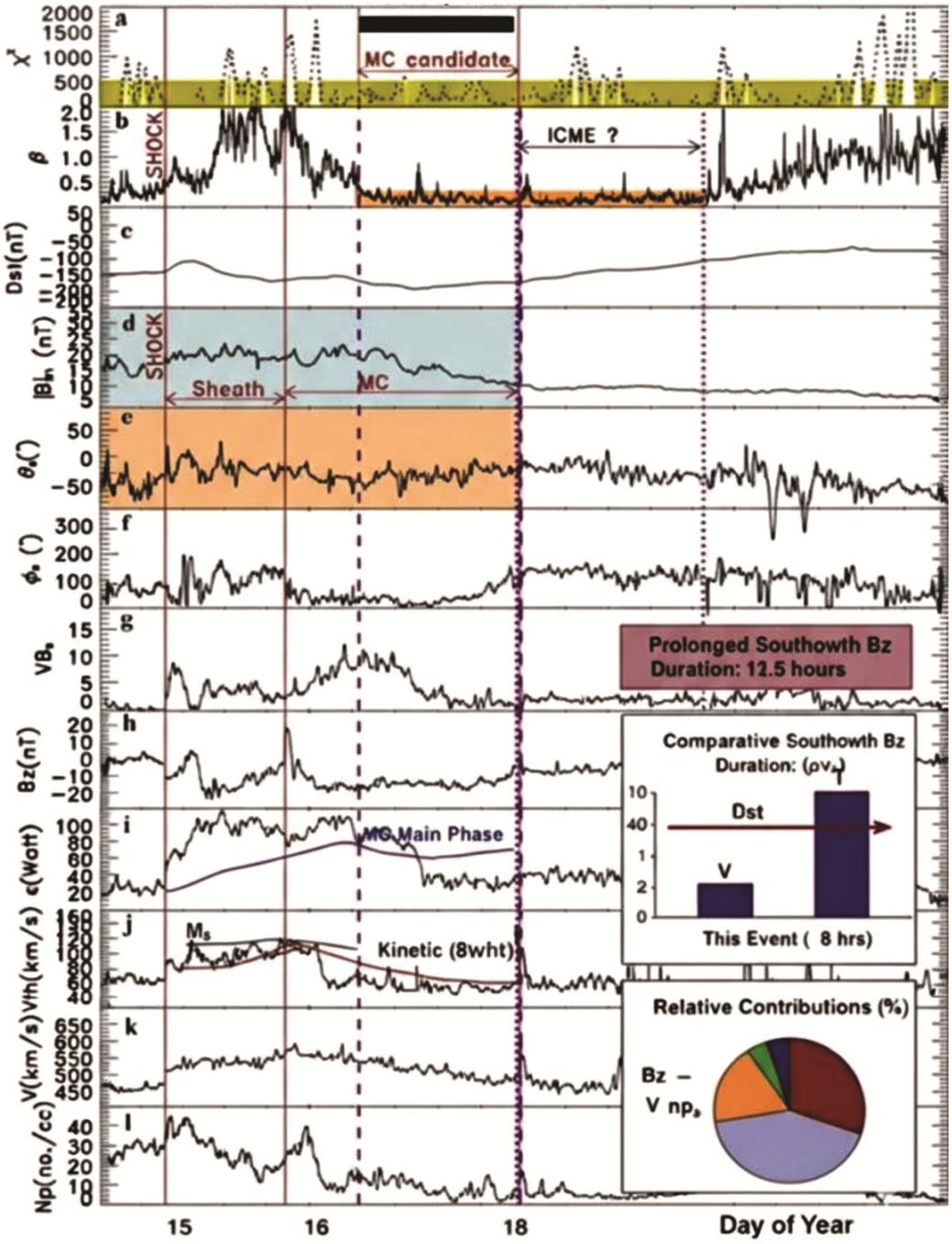

Fig. 3 — Magnetic and plasma profile of the March 2015 MC. Panels (a–j): χ^2 fit, proton (β), Dst, |B| and GSE angles, VBs, Bz, ε, $V_{Th,}$ V, and Dsw. Red lines indicate the IP shock and sheath; yellow highlights the MC candidate interval where $\chi^2 < 500$

3.2 The Fast CME-Driven Storm: 23 June 2015

3.2.1 The June 2015 "Summer Solstice" Geomagnetic Storm: Drivers and Dynamics

The intense geomagnetic storm of 21–23 June 2015, widely referred to as the "Summer Solstice Storm," represents one of the most significant space-weather events of Solar Cycle 24 in Fig. 4. It achieved a minimum Dst of -198 nT, securing its position as the second most severe event of the cycle, surpassed only by the March 2015 St. Patrick's Day storm[59]. The event was triggered by a fast, Earth-directed halo coronal mass ejection (CME) launched on 21 June at 03:12 UT from Active Region (AR) 2371, with a linear speed of approximately 1366 km/s as recorded

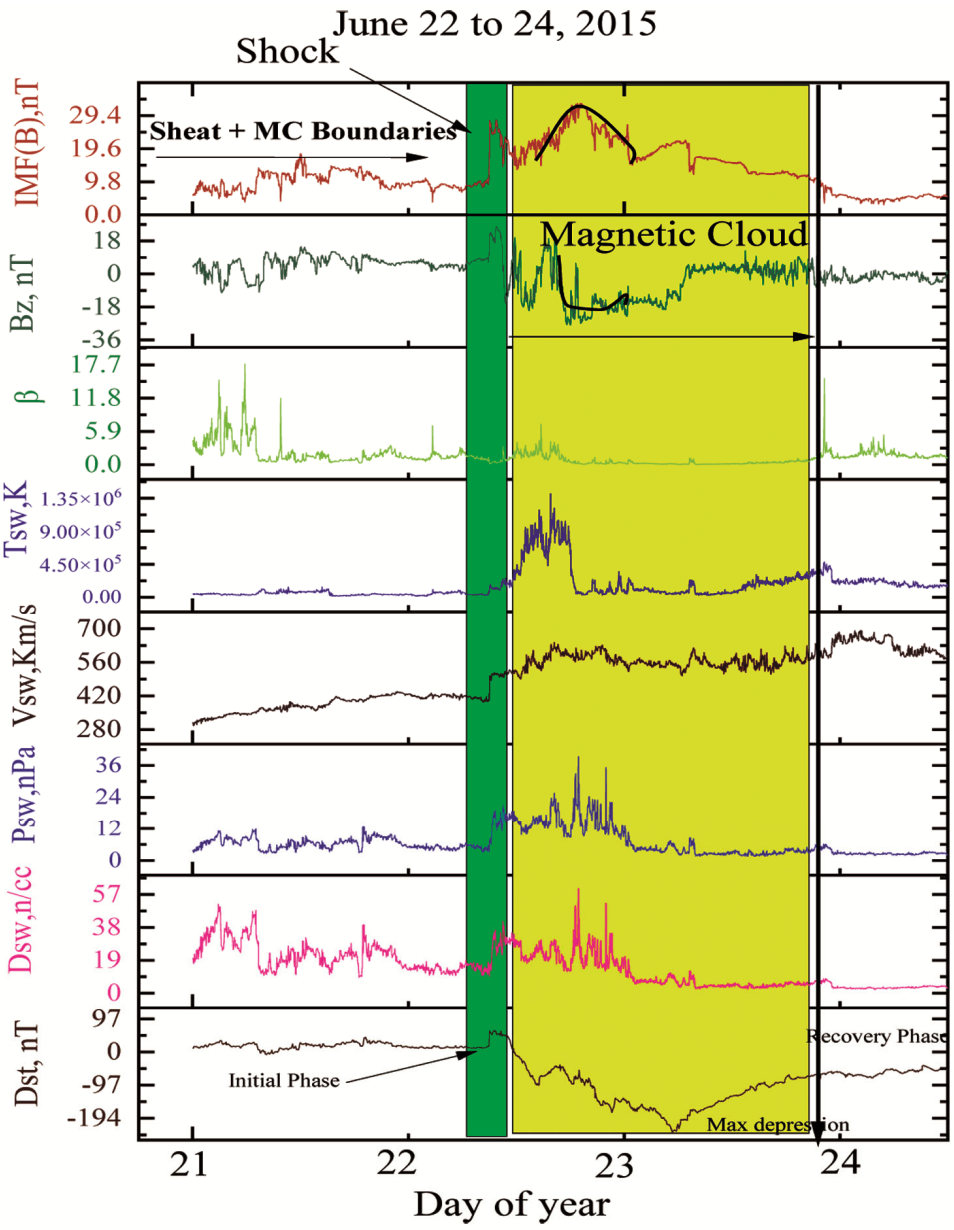

Fig. 4 — Overview of IMF and plasma parameters. Parameters from top to bottom: Dsw, Bz, β, Ey, Vsw, P_{dyn}, SYM-H, and Dst. Shaded intervals: green (sheath) and yellow (magnetic cloud). The MC characteristics (southward Bz, low β) define the Dst main-phase intensity

by the SOHO/LASCO coronagraphs. The subsequent interaction between this primary CME and successive ejecta from the same region created a complex interplanetary (IP) driver configuration, leading to a compressed and geo-effective sheath region and a coherent magnetic cloud at 1 AU[60]. Analysis of *in-situ* data from the Wind and ACE spacecraft confirms the arrival of a strong interplanetary shock at approximately 16:45 UT on 22 June, followed by an extended period of intense southward interplanetary magnetic field (IMF Bz) that drove the storm's main phase. The rapid solar wind speed exceeding 700 km/s, combined with an IMF magnitude greater than 40 nT, generated an exceptionally strong solar wind-magnetosphere coupling, quantified by the epsilon parameter. This event, characterized by extreme compression and magnetic reconnection efficiency, serves as a prime example of how CME-CME interactions can amplify geo-effectiveness, posing severe risks to technological infrastructure including satellite operations, navigation systems, and power grids[61,62].

3.2.2. Interplanetary Boundary Identification

In response to the transition between discrete IP regions, the event is characterized by three primary physical boundaries:

Shock Arrival and Sheath Start (~18:33–18:38 UT, 22 June): The leading IP shock reached Earth at approximately 18:35 UT, producing a distinct Sudden Storm Commencement (SSC). This is marked by simultaneous step-like enhancements in the interplanetary magnetic field (IMF) magnitude (B), solar wind speed (Vsw), and proton density (Dsw), alongside a rapid magnetospheric compression observed in the SymH index.

i Sheath-to-Magnetic Cloud (MC) Transition (~22:50 UT, 22 June): The turbulent sheath region, characterized by extreme dynamic pressure 36.8 nPa and large-amplitude Bz fluctuations reaching -29 nT, concluded as the high-frequency fluctuations gave way to the coherent structure of the MC. This boundary is defined by the transition to a low plasma beta (β) and a smooth, prolonged rotation of the magnetic field vector.

ii Magnetic Cloud Termination (Late 23 June): The MC interval, which facilitated sustained dayside reconnection, concluded as the proton temperature returned to ambient levels and the magnetic field strength decayed toward background values.

3.2.3. Storm Main Phase Chronology

The storm's main phase was driven by the sequence of the compressed sheath and the southward-directed MC. The Start of the Main Phase occurred at approximately 19:00 UT on 22 June, following the SSC and coinciding with the initial southward turning of the IMF Bz. The Main Phase Termination (Dst_{min}) was reached between 04:25 and 05:30 UT on 23 June, where the Sym-H index peaked at values between -195nT and -207 nT and the Kp index reached 8[62].

The global impacts of this interval were profound, including significant ionospheric Total Electron Content (TEC) variability and a 10^{o} declination shift at high-latitude stations like Barrow, Alaska. Because of its well-defined shock-sheath-MC sequence, the June 2015 storm serves as a benchmark for modeling CME-CME interactions and coupled magnetosphere-ionosphere-thermosphere responses shows in Table 1.

3.3 The Slow CME-Driven Storm: 20 December 2015 (Decoupling Kinematics from Geo-effectiveness: The Case of the December 2015 Storm)

The intense geomagnetic storm of 20 December 2015 (peak Dst ≈ -155 nT) serves as a critical paradigmatic example challenging the assumption that extreme geomagnetic disturbances. Figure 5 presents the *in situ* solar wind and geomagnetic conditions during the "slow CME-driven" storm of 20–21 December 2015, illustrating the decoupling of coronal mass ejection (CME) kinematics from geo-effectiveness. This analysis utilises high-resolution (1-minute) solar wind plasma and magnetic field data from the OMNI database, which combines measurements from the *Wind* and *ACE* spacecraft at the L1 Lagrange point[63]. The geomagnetic response is characterized using the Sym-H index, a high-time-resolution proxy for the Dst index that accurately tracks the ring current intensity[22]. Panel (e & f) plots the solar wind speed (Vsw, green line) and proton density (Dsw, brown line). The Vsw shows a modest increase from a background of ~400 km/s to a peak of ~550 km/s, which is not indicative of a fast, typically geoeffective CME (often >800 km/s)[64]. The sharp spike in Dsw at ~04:30 UT on 22 December marks

Table 1 — Summary of Interplanetary Structures and Geomagnetic Storm Phases during the June 2015 Event

Structure / Phase	Timeline (UT)	Key Interplanetary Signatures	Primary Geomagnetic Impact
IP Shock / SSC	22 June, 18:33–18:36	Sudden increase in IMF magnitude, solar wind speed (Vsw), and proton density (Dsw)	Sudden storm commencement; rapid magnetospheric compression (Initial Phase)
Sheath Region	22 June, 18:36–22:50	Strong IMF fluctuations, southward Bz down to −29 nT, high plasma density, extreme dynamic pressure (~36.8 nPa)	Rapid onset of main phase; enhanced solar wind–magnetosphere coupling
Magnetic Cloud (Ejecta)	Late 22 June – mid 23 June	Low plasma beta ($\beta \ll 1$), low proton temperature, smooth and prolonged southward Bz rotation	Peak storm intensity; maximum ring-current enhancement; Dst minimum of −198 nT
Storm Main Phase	June 22, 18:35 to June 23, 05:00		Steep decline in Dst/Sym-H index
Recovery Phase	Late 23 June – 24 June	Gradual return to ambient solar wind conditions	Slow decay of ring current; recovery of geomagnetic indices

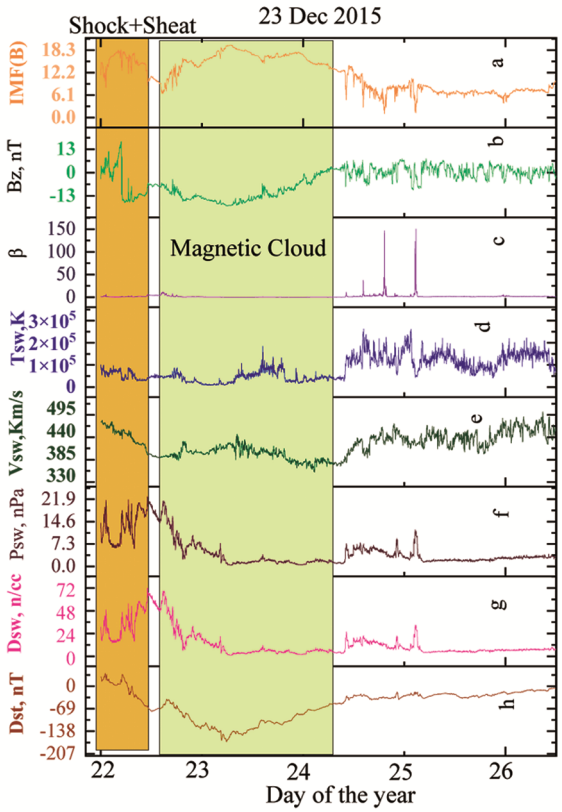

Fig. 5 — Solar wind and geomagnetic parameters. Top to bottom: |B|, Bz, Ey, Dsw, Vsw, P_{dyn}, SYM-H, and Dst. Shaded areas mark the shock–sheath and magnetic cloud. The Dst/SYM-H depression is driven by enhanced Vsw and prolonged southward Bz within the MC

the passage of the forward shock (S), with the subsequent region of high variability identified as the sheath a turbulent region of compressed plasma between the shock and the CME ejecta[65]. The sharp drop in Dsw to near-zero values after ~10:00 UT is a definitive signature of the magnetic cloud (MC), a region of low plasma beta and coherent, strong magnetic field characteristic of a flux rope structure[66]. Panel (a) displays the interplanetary magnetic field (IMF) components: the total field strength (B_{total}, pink line) and the north-south component (Bz, olive green fill). The Bt remains elevated above 25 nT throughout both the sheath and MC, confirming the passage of a strong, coherent structure. Critically, the Bz component, after fluctuating in the sheath, turns sharply southward (Bz< 0, blue) upon entry into the MC and remains steadily and intensely southward for approximately 10 hours (from ~10:00 UT to ~20:00 UT). This prolonged southward orientation is the essential condition for efficient magnetic reconnection at the dayside magnetopause, which drives energy injection into the magnetosphere[9]. Panel (h) shows the geomagnetic response via the Sym-H index. A small initial phase compression is followed by the onset of the main phase precisely coincident with the sustained southward Bz in the MC. The Sym-H index plunges to a minimum of –170 nT, corresponding to a G4 (Severe) geomagnetic storm on the NOAA scale[5]. The annotation explicitly links this depression to the driver. The figure thus provides direct observational evidence that the storm's severe intensity (Dst< -150 nT) originated not from rapid CME kinematics but from the internal magnetic structure of a moderately fast CME specifically, a strong, long-duration southward magnetic field within a well-defined magnetic cloud. This event has become a paradigmatic example in space weather, emphasizing that magnetic topology, rather than speed alone, is the dominant factor controlling CME geo-effectiveness[67].

3.4 The Late-Cycle Storm: 26 August 2018 (Anomalous Geo-effectiveness of the Slow CME-Driven Storm of August 2018)

The severe G3-class geomagnetic storm of 26 August 2018 (peak Dst -205 nT) represents a significant anomaly in the late declining phase of Solar Cycle 24, challenging conventional paradigms regarding the kinetic requirements for major space weather events. Despite originating from an exceptionally slow partial halo Coronal Mass Ejection (CME) on 20 August 2018 which propagated with a plane-of-sky speed of merely ~167 km/s this event evolved into one of the most geo-effective disturbances of the solar cycle. The CME arrival at Earth on 25 August (approx. 02:45 UT) was devoid of a distinct Sudden Storm Commencement (SSC), a characteristic consistent with the absence of a strong interplanetary shock typical of slow transients. However, the subsequent geomagnetic response defied the expectations usually associated with such low-momentum ejecta. The primary driver of this unexpectedly intense activity was identified as a highly structured Interplanetary CME (ICME) featuring a distinct magnetic cloud morphology. While solar wind speed, dynamic pressure, and plasma density remained relatively modest, the storm's efficacy was dictated by the internal magnetic orientation of the ejecta. Specifically, the event was catalyzed by a prolonged interval of strongly southward Interplanetary Magnetic Field (Bz), which reached a minimum of -17 nT and maintained a

steady negative orientation (approx. -12.9 nT) for several hours during the main phase. This sustained southward (Bz) facilitated highly efficient magnetic reconnection at the dayside magnetopause, enabling significant energy transfer into the magnetosphere despite the weak kinetic driver. This event underscores a critical observational gap: initial solar eruptions that appear benign to automated forecasting tools can manifest as severe hazards due purely to favorable magnetic coupling and duration. The ionospheric and thermospheric response to this energy injection was widespread, complex, and marked by significant longitudinal asymmetries. The storm induced global fluctuations in Total Electron Content (TEC), manifesting as mixed positive and negative storm phases that degraded satellite positioning accuracy (GPS errors >0.5m). Notably, intense ionospheric irregularities, including equatorial plasma bubbles (EPBs), were observed extending to atypically high latitudes for a solar minimum period, particularly over the Pacific and American sectors. These irregularities resulted in severe radio signal scintillation and cycle slips in navigation systems. Concurrently, the thermosphere underwent a drastic 300–500 % increase in neutral mass density, significantly heightening atmospheric drag and accelerating low-Earth orbit satellite decay. Collectively, these observations highlight a persistent and often underestimated space-weather hazard posed by slow-moving, magnetically favorable ICMEs, even during periods of quiescent solar activity.

The severe G4-class geomagnetic storm of 26 August 2018 (peak Dst -205 nT) represents a significant anomaly in the late declining phase of Solar Cycle 24 in Fig. 6, multi-panel analysis of the interplanetary drivers and geomagnetic response for the intense storm of 22–23 June 2015. Solar wind plasma and magnetic field data are from the OMNI database, combining measurements from the *Wind* and *ACE* spacecraft at the L_1 Lagrange point[68]. The geomagnetic response is quantified by the Dst index, derived from a network of low-latitude ground magnetometers[22]. In panel (a) The interplanetary magnetic field (IMF-B) shows an enhancement to approximately 9 nT; Panel (b) The crucial north-south component (Bz, in GSM coordinates) exhibits a significant and sustained southward excursion (Bz< 0); (c) The concurrent variation in the other IMF components indicates a smooth rotation, characteristic of an ordered magnetic structure. This configuration of a strong, southward field within a rotating framework is the essential precondition for efficient magnetic reconnection at the dayside magnetopause, the primary mechanism for solar wind energy transfer into the magnetosphere[4]. The solar wind plasma parameters reveal the event's kinematic structure: (d) the proton density shows an initial compression (>4.5 × 10^5 cm^{-3}) followed by a sharp drop, while (e) the bulk speed displays a characteristic declining profile from ~600 km/s to ~200 km/s. This combination of strong, rotating magnetic fields, low plasma density, and declining velocity is the definitive signature of a magnetic cloud (MC) a coherent interplanetary coronal mass ejection (ICME) flux rope structure with low plasma beta[5]. The grey-shaded region demarcates this MC interval. (f) The geomagnetic Dst index response shows a severe depression, reaching a minimum of -225 nT. This qualifies the event as a major (G4–Severe) geomagnetic storm on the NOAA space weather scale[9]. The precise temporal alignment demonstrates

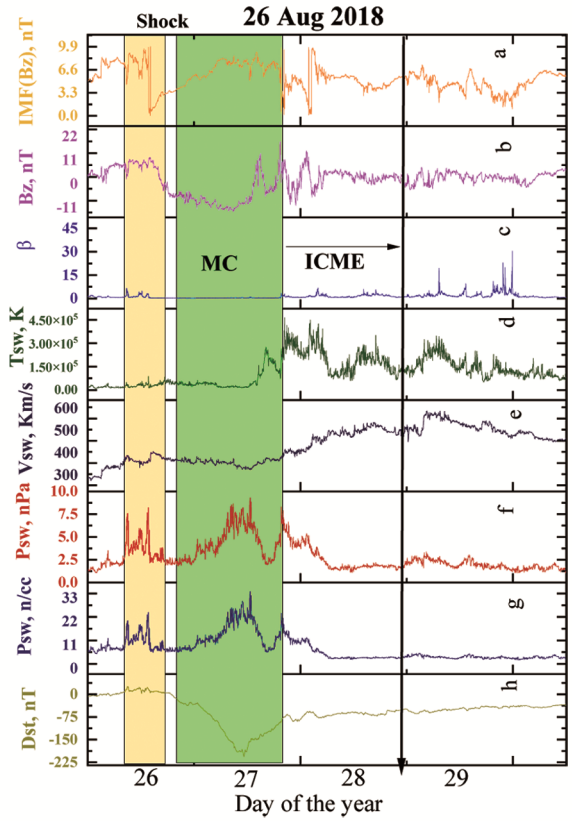

Fig. 6 — Interplanetary and geomagnetic time series. Top to bottom: |B|, Bz, β, Ey, Vsw, P_{dyn}, Dsw, and Dst. The shaded area denotes the shock and sheath. The Dst depression results from enhanced solar wind speed and prolonged southward Bz

Table 2 — Comparison Table of Four Major Geomagnetic Storms[70,28]

Event (Storm Peak Date)	CME Parameters (Speed, Origin)	Key Solar Wind Features at L1	Minimum Dst (nT) & Storm Class	Notable Impacts
"St. Patrick's Day" Storm (17 March 2015)	Double-CME Event 1st: Slow (~600 km/s), 15 Mar 2nd: Fast (~1400 km/s), 15 Mar Origin: Active Region 12297	Prolonged strong southward Bz: ~-20 nT for ~12 hours High speed: Peak ~700 km/s Dynamic Pressure: High but variable	-223 nT (G4 - Severe)	Widespread aurora to mid-latitudes (e.g., Arizona, UK) HF radio blackouts, voltage alarms in power grids, satellite drag
June 2015 Storm (22-23 June 2015)	Moderate, stealthy CME Launched 19 June No clear low-coronal signature Origin: Faint eruption near a coronal hole	Moderately strong Bz: ~-15 to -20 nT for ~9 hours High speed: Sustained ~650 km/s from CME + coronal hole stream Combined influence	-195 nT (G4 - Severe)	Strong auroral displays, GPS signaldegradation at mid-latitudes Demonstrated "stealth CME" hazard
December 2015 Storm (20 December 2015)	Moderately fast CME Launched 16 Dec (~800 km/s) Origin: AR 12473 Arrived 19 Dec	Intense but short Bz: Brief spikes to ~-30 nT, but main phase Bz ~-15 nT for ~6 hours High speed: ~650 km/s Density: High	-155 nT (G3 - Strong)	Bright aurora seen in US Midwest and Europe Minor technological impacts
August 2018 Storm (26 August 2018)	Slow, weak CME Launched 20 Aug. (~500 km/s) Overtaken by a fast Coronal Hole High-Speed Stream (CH HSS)	Prolonged, moderate Bz: ~-10 to -15 nT for >24 hours due to CH HSS Very high speed: Peak >700 km/s from HSS Long duration (>3 days)	-174 nT (G3 - Strong)	Extended period of active geomagnetic conditions Auroras at high latitudes for multiple nights Showcased CME-HSS compound effect

that the storm's main phase is directly and exclusively driven by the extended interval of intense southward IMF Bz embedded within the magnetic cloud. This event serves as a clear observational example where the extreme geo-effectiveness of a CME is governed not by exceptional kinematic properties (e.g., high speed) but by its internal magnetic topology specifically, the presence of a long-duration, strongly southward magnetic field within a well-defined flux rope[69].

4 Conclusion

Four of the most intense geomagnetic storms that occurred during the comparatively weak Solar Cycle 24 were examined, revealing substantial diversity in their solar and interplanetary drivers. The analysed events demonstrate that major geomagnetic storms can be produced by a wide range of CME characteristics, from fast eruptions generating strong sheath regions (e.g., the June 2015 storm) to slower CMEs whose geo-effectiveness was dominated by well-organised magnetic cloud structures (e.g., the December 2015 and August 2018 storms). In several cases, interactions with background solar wind structures, particularly coronal hole high-speed streams (HSSs), played a crucial role in enhancing storm intensity and duration.

A comparative analysis of the four events shows that comparison Table 2 in the dominant controlling factor of storm intensity was not CME speed, but the strength and persistence of the southward interplanetary magnetic field (Bz) at 1 AU. All storms were characterized by sustained southward Bz intervals, which enabled efficient solar wind–magnetosphere coupling and drove intense ring current development. Notably, the August 2018 storm triggered by a slow CME occurring late in the declining phase of Solar Cycle 24 produced a major geomagnetic response due to the prolonged southward Bz resulting from CME–HSS interaction. This finding highlights that significant space weather hazards can arise even during periods of low solar activity and from seemingly weak solar eruptions.

These results have important implications for space weather forecasting. Reliance on CME speed, flare class, or shock strength alone is insufficient to reliably predict geomagnetic storm severity. Instead, accurate forecasting requires improved prediction of the internal magnetic field configuration of ICMEs, particularly the magnitude and duration of the southward Bz component, which remains one of the most challenging aspects of space weather modeling.

Future work will focus on event-specific, data-constrained magneto hydrodynamic (MHD) simulations that track CME evolution from the low corona to 1 AU. Such modeling efforts, combined with multi-point in situ observations, are essential for understanding how CME magnetic structures evolve in interplanetary space and for advancing predictive capabilities of highly geo-effective geomagnetic storms.

References

1 Webb D F & Howard T A, *Living Rev Sol Phys*, 9 (2012) 3.
2 Chen P F, *Living Rev Sol Phys*, 8 (2011) 1.
3 Gonzalez W D, Joselyn J A, Kamide Y, Kroehl H W, Rostoker G, Tsurutani B T & Vasyliunas V M, *J Geophys Res Space Phys*, 99 (A4) (1994) 5771.
4 Sugiura M, *Ann Int Geophys Year*, 35 (1964) 945.
5 Dungey J W, *Phys Rev Lett*, 6 (2) (1961) 47.
6 Gonzalez W D & Tsurutani B T, *Planet Space Sci*, 35 (9) (1987) 1101.
7 Burton R K, McPherron R L & Russell C T, *J Geophys Res*, 80 (31) (1975) 4204.
8 Tsurutani B T, Gonzalez W D, Tang F, Akasofu S I & Smith E J, *J Geophys Res: Space Phys*, 93 (A8) (1981) 6673.
9 Pesnell W D, *Space Weather*, 14 (1) (2016) 10.
10 Gopalswamy N, Akiyama S, Yashiro S & Mäkelä P, In *Magnet Coupling between the Interior and Atmosphere of the Sun* (Springer, New Delhi), 2015, p. 289.
11 Gopalswamy, N *et al*., *J Phys: Confer Ser*, 642 (1) (2015) 012012.
12 Kataoka R, *et al*., *Geophys Res Lett*, 42 (13) (2015) 5155.
13 Nandy D, Martens P C & Obridko V, *Solar Phys*, 296 (3) (2021) 54.
14 Liu Y D, *et al*., *Nature Comm*, 6 (2015) 7599.
15 Kilpua E K J, *et al*., *Sol Phys*, 292 (1) (2017) 11.
16 Wu C C & Lepping R P, *Sol Phys*, 291 (1) (2016) 265.
17 Lugaz N, Farrugia C J, Huang C L & Spence H E, *Geophys Res Lett*, 42 (12) (2015) 4694.
18 Scolini C, *et al*., *Astrophys J Suppl Ser*, 247 (1) (2020) 21.
19 Zhang J, *et al*., *J Geophys Res: Space Phys*, 112 (2007) (A10).
20 Sugiura M & Kamei T, *IAGA Bulletin*, 40 (1991) 1.
21 King J H & Papitashvili N E, *J Geophys Res: Space Phys*, 110 (2005) (A2).
22 Garg S, Tripathi O P & Kumar S, *Ind J Pure & Appl Phys,* 63 (2025) 1032.
23 Loewe C A & Prölss G W, *J Geophys Res: Space Phys*, 102 (1997) (A7) 14209.
24 Echer E, Gonzalez W D, Tsurutani B T & Gonzalez A L, *J Geophys Res: Space Phys*, 113 (2008) (A5).
25 Kumar S, Tripathi O P, Sharma R & Verma P L, *Journal of Physics Conf.Series,* 2576 (1) (2023) 012015.
26 Kane R P, *J Geophys Res: Space Phys*, 110 (2005) (A2).
27 Kumar S, Garg S, Thakur P S, *et al., Rend Fis Acc Lincei,* 1 (2026) 1.
28 Yermolaev Y I, *et al*., *J Geophys Res: Space Phys*, 117 (2012) (A8).
29 Yashiro S, Gopalswamy N, Michalek G, St Cyr O C, Plunkett S P, Rich, N B & Howard R A, *J Geophys Res: Space Phys*, 109 (2004) (A7).
30 Gopalswamy N, Yashiro S, Michalek G, Stenborg G, Vourlidas A, Freeland S & Howard R, *Earth Moon Planets*, 104 (1) (2009) 295.
31 Kilpua E K J, Olspert N, Grigorievskiy A, Käpylä M J, Tanskanen E I, Miyahara H & Kataoka R, *Astrophys J*, 806 (2) (2015) 272.
32 Kilpua E K J, Good S W & Dresing N, *Sol Phys*, 296 (6) (2021) 1.
33 Kumar S, Sharma R, Tripathi O P & Verma P L, *J Scientif Res,* 16 (1) (2024) 107.
34 Tsurutani B T, Gonzalez W D, Tang F, Akasofu S I & Smith E J, *J Geophys Res: Space Phys*, 93 (1988) (A8) 8519.
35 Kilpua E K J, Lumme E, Andreeova K, Isavnin A & Koskinen H E J, *J Geophys Res: Space Phys*, 122 (7) (2017) 7238.
36 Lepping R P, Jones J A &Burlaga L F, *J Geophys Res: Space Phys*, 95 (1990) (A8) 11957.
37 Richardson I G & Cane H V, *Sol Phys*, 264 (1) (2010) 189.
38 Kamide Y, *et al*., *J Geophys Res: Space Phys*, 103 (1998) (A8) 17705.
39 Tripathi O P & Verma P L, *IJAR,* 3 (5) (2013) 50.
40 Kilpua E K J, Koskinen H E J & Pulkkinen T I, *Living Rev Sol Phys*, 18 (1) (2021) 1.
41 Lepping R P, Wu C C & Berdichevsky D B, *Ann Geophys*, 23 (8) (2005) 2687.
42 Tripathi O P, Pandey V & Verma P L, *IJAR,* 9 (6) (2019) 26.
43 Smith Z K, *et al*., *J Geophys Res: Space Phys*, 123 (4) (2018) 2599.
44 Turner J M, *et al.*, *Geophys Res Lett*, 44 (10) (2017) 4504.
45 Gopalswamy N, *et al*, *Space Weather*, 13 (9) (2015) 535.
46 Akasofu S I, *J Geophys Res: Space Phys*, 121 (1) (2016) 13.
47 Hu Q & Sonnerup B U Ö, *J Geophys Res: Space Phys*, 107 (2002) (A10) 1142.
48 Al-Haddad N, *et al.*, *Sol Phys*, 284 (1) (2013) 129.
49 Pulkkinen A, *et al*., *Space Weather*, 15 (7) (2017) 828.
50 MacDonald E A, *et al*., *Space Weather*, 13 (9) (2015) 548.
51 Henderson M G, *et al*., *J Geophys Res: Space Phys*, 123 (3) (2018) 2100.
52 Astafyeva E, *et al*., *Geophys Res Lett*, 42 (21) (2015) 9156.
53 Olwendo O J, *et al*., *Space Weather*, 16 (9) (2018) 1184.
54 Boteler D H, *Space Weather*, 17 (10) (2019) 1427.
55 Käki S, *et al*., *Space Weather*, 14 (10) (2016) 713.
56 Coster A J & Skone S, In *Position, Navigation, and Timing Technologies in the 21st Century* Wiley-IEEE Press (2017).
57 Riley P & Love J J, *Space Weather*, 15 (1) (2017) 53.
58 Hapgood M, *Space Weather*, 15 (5) (2017) 650.
59 Gopalswamy N, *et al*., *Sol Phys*, 291 (2) (2016) 327.
60 Akasofu S I, *Space Sci Rev*, 28 (2) (1981) 121.
61 Baker D N, *et al*., *Space Weather*, 14 (12) (2016) 1037.
62 Eastwood J P, *et al*., *Risk Analys*, 37 (2) (2017) 206.
63 Sibeck D G & Papitashvili N E, *Magnetospher Curr Syst Geophys Monogr Ser*, 118 (2000) AGU.
64 Gopalswamy N, *Climate and Weather of the Sun-Earth System (CAWSES)*, Tokyo, 2009 77–120.
65 Tsurutani B T & Gonzalez W D, *Magnet Storms, Geophys Monogr Ser*, 98 AGU (1997) 77.
66 Lynch B J, *et al*., *Space Weather*, 17 (10) (2019) 1427.
67 Lee C O, *et al*., *Astrophys J*, 884 (2) (2019) 120.
68 TsurutaniB T & Gonzalez W D, *Magnet Storms*, *Geophys Monogr Ser*, 98 (1997) 77.
69 Dimmock A P, *et al*., *J Geophys Res Space Phys*, 124 (5) (2019) 3004.